

# Big Bang Nucleosynthesis Limits and Relic Gravitational Waves Detection Prospects

Tina Kahniashvili,<sup>1,2,3,\*</sup> Emma Clarke,<sup>1,†</sup> Jonathan Stepp,<sup>1,‡</sup> and Axel Brandenburg<sup>4,5,2,1,§</sup>

<sup>1</sup>*McWilliams Center for Cosmology and Department of Physics,  
Carnegie Mellon University, Pittsburgh, PA 15213, USA*

<sup>2</sup>*School of Natural Sciences and Medicine, Ilia State University, 0194 Tbilisi, Georgia*

<sup>3</sup>*Abastumani Astrophysical Observatory, Tbilisi, GE-0179, Georgia*

<sup>4</sup>*Nordita, KTH Royal Institute of Technology and Stockholm University, 10691 Stockholm, Sweden*

<sup>5</sup>*The Oskar Klein Centre, Department of Astronomy,  
Stockholm University, AlbaNova, SE-10691 Stockholm, Sweden*

(Dated: June 22, 2022)

We revisit the big bang nucleosynthesis (BBN) limits on primordial magnetic fields and/or turbulent motions accounting for the decaying nature of turbulent sources between the time of generation and BBN. This leads to larger estimates for the gravitational wave (GW) signal than previously expected. We address the detection prospects through space-based interferometers and pulsar timing arrays or astrometric missions for GWs generated around the electroweak and quantum chromodynamics energy scale, respectively.

Gravitational radiation from the early universe propagates almost freely throughout the universe's expansion and primordial gravitational waves (GWs) reflect a precise picture of the very early universe. Detection of these GWs is a promising tool that would open new avenues to understand physical processes at energy scales inaccessible to high energy particle physics experiments but accessible to astrophysical observation [1].

There are several milestones of modern cosmology, proven through cosmic microwave background (CMB) anisotropies and large scale structure statistics. In particular, the light element abundances allow us to reconstruct the picture of big bang nucleosynthesis (BBN), but leave several puzzles prior to BBN (matter-antimatter asymmetry, dynamics of the universe at the very beginning, nature of dark matter, etc) unsolved. These unknowns will be reflected in the variety of relic GW characteristics, including not only the strength of the signal and its spectral shape, but also its polarization. Indeed detection of GW polarization is a unique tool to test fundamental symmetries at these extremely high energies. If GWs originated from parity violating sources in the early universe, they will be circularly polarized and, unlike the CMB, GW polarization will exist at the basic background and *not just the perturbation* level; see Ref. [2] for pioneering work and see Refs. [3–8] for recent studies. This is analogous to the GWs produced via Chern-Simons coupling [9, 10]. If detected, the GW polarization can be a *direct* measure of the deviations from the standard model (SM) [11–13]. One of the major goals of this Letter is to determine whether these circularly polarized GWs and their polarization are potentially detectable in the upcoming early-universe GW observation missions [14].

The strategy to detect the stochastic GW polarization is based on anisotropy [15] induced, for example, through our proper motion [16, 17]. Despite promising detection prospects for stochastic GWs through pulsar timing arrays (PTAs), which are potentially sensitive to GWs generated around the quantum chromodynamic (QCD) energy scale, detection of the polarization degree remains problematic.

BBN data (based on light element abundances<sup>1</sup>) impose an upper limit on the universe's expansion rate, e.g., the Hubble parameter,  $H = d\ln a/dt_{\text{phys}}$  (with physical time  $t_{\text{phys}}$  and scale factor  $a$ ), and correspondingly, on additional relativistic species such as massless (or ultrarelativistic) hypothetical particles, early stage dark energy (or any bosonic massless field), dark radiation, electromagnetic fields or early-universe plasma motions (turbulence), relic GWs, etc [20–26]. Conventionally, the energy density of these additional relativistic components is characterized in terms of the *effective number of relativistic species*,  $N_{\text{eff}}$ . The SM predicts for neutrino species  $N_{\text{eff}}^{(\nu)} = 3.046$ , which is slightly larger than 3 because neutrinos did not decouple instantaneously and were still able to interact with electrons and positrons near electron-positron annihilation [27]. Other additional relativistic components contribute  $\Delta N_{\text{eff}} = N_{\text{eff}} - N_{\text{eff}}^{(\nu)}$  to this *effective* neutrino count. Notably, the presence of additional relativistic components does not spoil the time dependence of the scale factor during the radiation-dominated epoch, but it does affect the Hubble parameter and Hubble time scale,  $H^{-1}$ . The joint analysis of CMB measurements and BBN light element abundances put  $N_{\text{eff}} = 2.862 \pm 0.306$  at 95% confidence [28]. Using the upper bound of this error interval ( $N_{\text{eff}} = 3.168$ ), we express the maximum ratio

\*Electronic address: tinatin@andrew.cmu.edu

†Electronic address: emmaclar@andrew.cmu.edu

‡Electronic address: jdstepp@andrew.cmu.edu

§Electronic address: brandenb@nordita.org

<sup>1</sup> In what follows we neglect the effects of the strong primordial magnetic field on BBN dynamics as discussed in Refs. [18, 19]

of additional components of energy density  $\rho_{\text{add}}$  to the radiation energy density  $\rho_{\text{rad}}$  at the BBN temperature as  $\rho_{\text{add}}/\rho_{\text{rad}} \simeq 0.0277 (\Delta N_{\text{eff}}/0.122)$ , normalized around  $\Delta N_{\text{eff}} = 0.122$ . The maximum value of this ratio is limited by the combined CMB and BBN data. We note that this upper bound coincides with the constraint on the GW contribution to the radiation energy density found in Ref. [29] using CMB and BBN data combined with limits from NANOGrav and late-time measurements of the expansion history. Interestingly, the light element abundances (with the bounds on  $N_{\text{eff}}$ ) impose limits on the lepton asymmetry in the universe [30] that might result in primordial chiral magnetic fields [31] and correspondingly serve as a source for polarized GWs [8].

In this Letter we address the BBN bounds from the point of view of early-universe anisotropic stress (namely primordial magnetic fields and turbulent sources) and the induced GW signal. Inhomogeneous magnetic fields are known to affect the primordial lithium abundance [32]. Here, however, we are particularly interested in the strength, the spectral shape, and the polarization degree of the induced GWs. Violent processes in the early universe might lead to the development of turbulence. In particular, first order electroweak (EW) and QCD phase-transition bubble collisions and nucleation might lead to turbulent plasma motions [33–36], or, alternatively, turbulence can be induced by primordial magnetic fields coupled to the cosmological plasma [37–41]. The stochastic GW background from these turbulent sources has been studied for decades now; see Refs. [36, 42, 43] for pioneering works and Ref. [44] for a review and references therein.

Both analytical and numerical studies suggest that a strong enough gravitational radiation signal (when and if the total energy density of the source is a substantial fraction of the total (radiation) energy density,  $\rho_{\text{rad}}$ , at the moment of the GW generation, characterized by the temperature,  $T_*$ , and the number of relativistic degrees of freedom,  $g_*$ , where here and below an asterisk denotes the generation moment) is detectable by space-based missions, such as the Laser Interferometer Space Antenna (LISA) (for GWs generated around the EW energy scale) [44], or by PTAs, such as NANOGrav [45], and astrometric missions such as GAIA [46] (for GWs generated around the QCD energy scale). Notably, the NANOGrav collaboration recently announced strong evidence for a stochastic GW signal [45] that might be associated with primordial sources [47]. On the other hand, when estimating the strength of the GW signal, the maximum allowed source energy density was assumed to be determined by the BBN bounds discussed above (i.e., not exceeding a few percent of the total radiation energy, i.e.  $\mathcal{E}_{\text{turb}} = \zeta \rho_{\text{rad}}$  with the parameter  $\zeta$  being in general time-dependent and being a few per cent at BBN).

Due to weak coupling between gravity and matter (i.e., the smallness of Newton’s constant  $G$ ), the GW generation from any turbulent source is characterized by low efficiency and, consequently, the ratio  $\zeta$  of turbu-

lent source energy density to the total radiation energy is not affected by the emission of gravitational radiation. In other words, the energy radiated in GWs will not induce substantial damping of the turbulent energy density. Moreover, if turbulent decay processes are discarded (i.e., velocity and magnetic fields are “frozen-in” to the primordial plasma),  $\zeta$  is unchanged during the radiation-dominated epoch. Applying this logic to the BBN bounds, the few percent limit was applied *a priori* to much earlier time scales when GWs were generated. As it was seen in simulations [7, 49], the GW energy density reaches a maximum and stays unchanged after a short time. Thus, only  $\zeta$  at *the moment of the source activation* (i.e., GW generation) matters.

In the case of decaying turbulence, the situation is different:  $\zeta$  is time dependent and the decay rate is determined by the specific model of turbulence. Decaying turbulence leads to a power-law decay  $\mathcal{E}_{\text{turb}}(t) \propto (t/t_*)^{-p}$ , and a growth of the correlation length  $\xi_{\text{turb}}$  by an inverse cascade mechanism such that  $\xi_{\text{turb}} \propto (t/t_*)^q$ , where  $t = \int dt_{\text{phys}}/a$  is the conformal time and the parameters  $p$  and  $q$  depend on the properties of the turbulence (e.g., in helical turbulence  $p = q = 2/3$ , while for non-helical magnetically dominated turbulence  $p = 1$  and  $q = 1/2$ , but other variants are possible). The scaling exponent  $q$  may reflect the presence of an underlying conservation law (helicity conservation, Loitsiansky integral) and is also determined by the nature of turbulence (kinetically or magnetically dominated). The combined values of  $p$  and  $q$  for a particular process can be summarized by the parameter  $\beta = p/q - 1$ , which characterizes the decay of the spectral peak of magnetic energy [50]. Partially helical magnetic fields are also described by their fractional helicity, i.e., the ratio of the magnetic helicity to its maximal value,  $\epsilon_{M,*} < 1$ . Due to this decay, the BBN bound allows larger values of  $\zeta$  at the moment of GW generation, making the GW signal stronger. The maximum allowed energy density of turbulent sources that satisfy the BBN limits will be different at the EW and QCD energy scales (EW turbulence has a longer decay period, allowing higher values for the initial energy density that still satisfies the BBN bounds).

Figure 1 shows the bounds on the strength of the magnetic fields at their generation (EW or QCD scales) determined such that the strength does not exceed the upper limit of the comoving field strength at BBN [51] and is above the lower observational bounds on the field strength at recombination. We see that allowed values for the magnetic fields at the moment of generation (upper left end of the lines) are not constrained to microGauss field strength, as it was claimed previously based on BBN bounds without accounting for decaying turbulence [52]. In fact, if we were previously considering an Alfvén speed  $v_A$  or characteristic velocities of 0.2–0.3 (in units of the speed of light), the new limits possibly imply  $v_A \rightarrow 1$  [49]. Obviously, in this case we deal with relativistic turbulence that might be characterized by different decay laws or efficiency to generate GWs. However, recent rel-

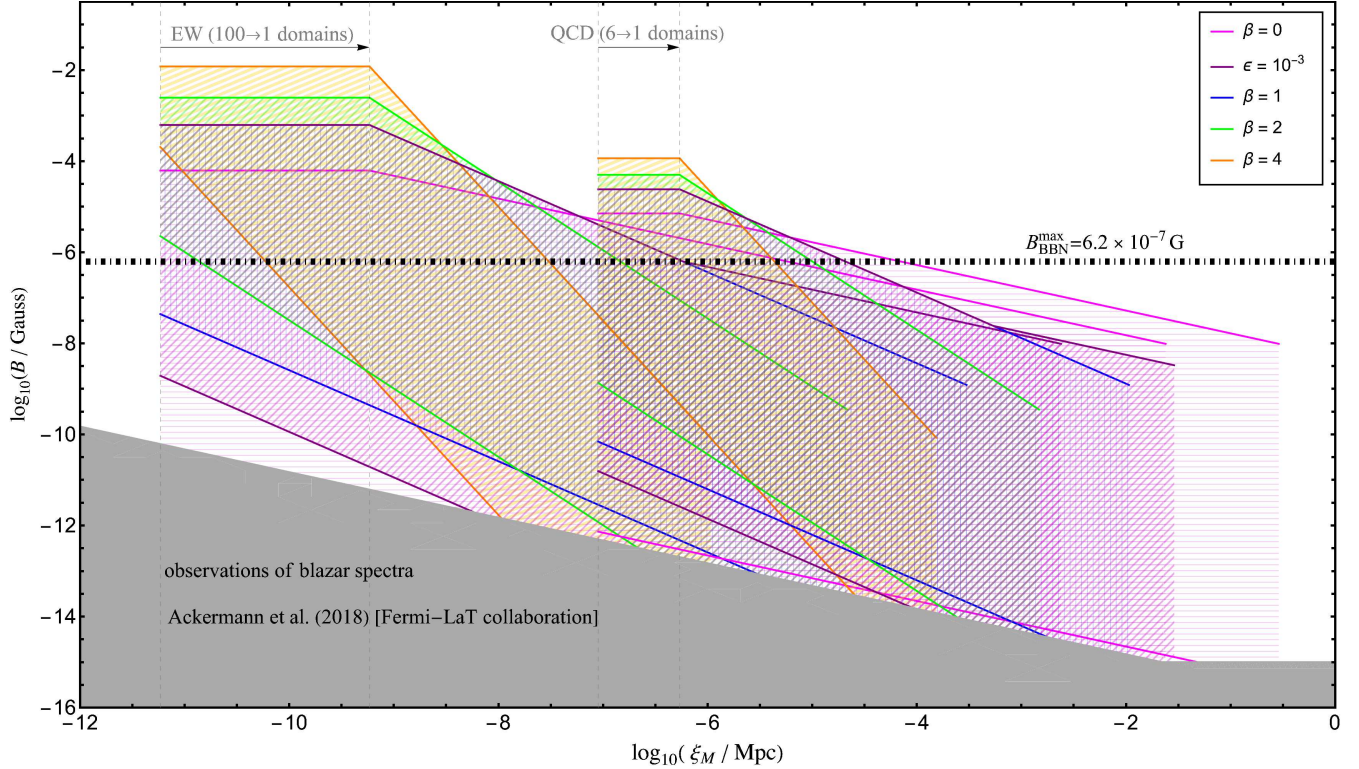


FIG. 1: Possible turbulent evolution of the comoving magnetic field strength  $B$  (decaying with time) and correlation length  $\xi_M$  (increasing with time) from generation at the EW and QCD scales in the cases of fully helical ( $\beta = 0$ ), nonhelical ( $\beta = 1, 2, 4$ ), and partially helical (with  $\epsilon_{M,*} = 10^{-3}$ ) MHD turbulence. Upper limits on the correlation length are determined by the size of the horizon and number of domains (bubbles) at generation, ranging from 1 to 6 (at QCD) or 100 (at EW), depending on the phase transition modeling. Lines terminate (on the right) at recombination ( $T = 0.25$  eV). The upper limit of the comoving field strength at BBN ( $T = 0.1$  MeV) is indicated by the black dot-dashed line. Regimes excluded by observations of blazar spectra [48] are marked in gray. The hatched regions correspond to possible trajectories bounded by an (upper) limit from BBN and a (lower) limit from the blazar spectra.

ativistic turbulence numerical simulations [53] show that the basic properties of turbulence decay are preserved, including non-helical inverse cascading. Also, following arguments of Ref. [42], the non-relativistic description of turbulent sources results in an underestimation of the signal.

Below we present the first simulations of the GW signal from such strong turbulence sources. We use the PENCIL CODE [54, 55] to simulate magnetohydrodynamic (MHD) turbulence in the early universe by computing the stochastic GW background and relic magnetic fields [49]. Turbulence is driven by applying an electromagnetic force that is  $\delta$ -correlated in time and has the desired spatial spectrum. We vary the forcing strength and adjust the viscosity such that the smallest length scales in the simulation are sufficiently well resolved to dissipate the injected energy near the highest available wavenumber. We perform runs for the QCD and EW energy scales; see Ref. [51] for a table summarizing the eight runs presented in this Letter.

The GW detection prospects are strongly affected by the characteristic frequency ranges and thus the energy-containing wave number of the source. More precisely,

the GW spectrum peaks at the comoving angular frequency  $\omega_{\text{peak}} = (2\pi f_{\text{peak}}) = 2k_0$ , where  $k_0$  is the initial peak wave number of the source energy density spectrum (in natural units  $c = 1$ ). The inertial wave number is determined by the turbulent eddy size ( $k_0 = 2\pi/L$ ), and if we assume that turbulence arises from phase transitions, the eddy size may be associated with the bubble size [56]. Independently of the nature the turbulence, the typical length scale is limited by the Hubble scale. In what follows, we use the characteristic wave number  $k_0$  normalized by the Hubble wave number  $H_*$ .

The energy density of early-universe turbulent sources is determined by the efficiency of converting the available radiation energy into turbulent energy. In the case of first-order phase transitions, it can be expressed in the terms of the parameter  $\alpha = \rho_{\text{vac}}/\rho_{\text{rad}} = 4\rho_{\text{vac}}/3(\rho + P)$  (with  $\rho$  and  $P$  being the plasma energy density and pressure, respectively) – the ratio between the latent heat (false vacuum energy) density and the plasma radiation energy density (which is determined at the phase transition temperature [36]).  $\alpha \sim a$  few corresponds to extremely strong phase transitions. Ref. [57] discusses a few beyond-SM models, which could include first-order phase

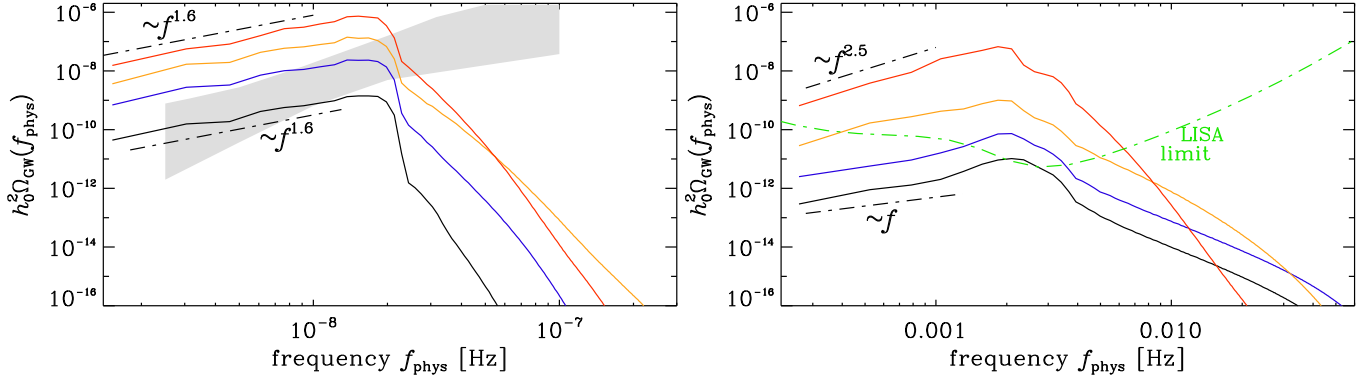


FIG. 2: GW energy spectra (per logarithmic frequency interval),  $h_0^2 \Omega_{\text{GW}}(f)$ , for both the QCD Runs a–d (left) and the EW Runs A–D (right) scales shown in red, orange, blue, and black, respectively.

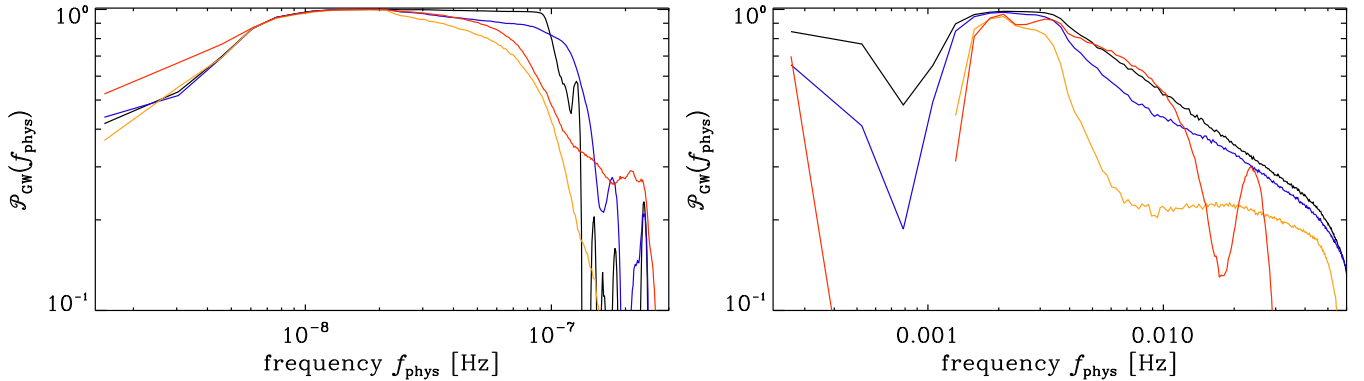


FIG. 3: Polarization spectra,  $\mathcal{P}_{\text{GW}}(f)$ , for the QCD Runs a–d (left) and the EW Runs A–D (right) scales [51] shown in red, orange, blue, and black, respectively.

transitions, and some of these models predict  $\alpha \gtrsim 1$  for specific ranges of their parameter spaces. In particular, the addition of a 6-dimensional term to the Higgs potential [58] or the addition of a singlet scalar field [59] allow for these particularly strong phase transitions. The induced turbulence can then be characterized by the velocity  $v_i = 1/\sqrt{1 + (\rho + P)/(2\mathcal{E}_i)}$ , which refers either to the turbulent velocity  $v_T$  or the effective Alfvén velocity  $v_A$ , and  $\mathcal{E}_i$  refers to either the kinetic,  $\mathcal{E}_K$ , or magnetic,  $\mathcal{E}_M$ , energy density. By defining the efficiency coefficient  $\kappa \equiv \kappa(\alpha) \in (0, 1)$  (which increases with  $\alpha$ ), i.e., the fraction of vacuum energy that is transformed into  $\mathcal{E}_K$  or  $\mathcal{E}_M$ , rather than into heat [42], we recover *relativistic expressions* for turbulent motions,  $v_T = 1/\sqrt{1 + 4/(3\kappa\alpha)}$  [60], and the Alfvén velocity,  $v_A = 1/\sqrt{1 + (4/3)\rho/(2\mathcal{E}_M)}$  [61],<sup>2</sup> while previous studies (see Ref. [44] for a review and references therein) assumed non-relativistic motions.

The additional relativistic degrees of freedom in the early universe due to the addition of the energy densities of the turbulent sources can be subsumed into  $\Delta N_{\text{eff}}$ . This increase in  $N_{\text{eff}}$  increases the CMB-inferred value of the Hubble constant,  $H_0$ , helping to reduce the tension with late-universe values. A value of  $\Delta N_{\text{eff}} \sim 0.4$  could alleviate the Hubble tension [62]. Interestingly, it has been shown that the recent NANOGrav results may also favor a larger value of  $N_{\text{eff}}$  [63] if the signal arises in the early universe. Even though large values of  $\alpha$  are not restricted by currently available BBN or other observational data, we limit ourselves by  $\alpha_{PT} \leq 1$  that was addressed previously in several studies, see Ref. [1] and references therein.

In Figure 2, we present GW spectra (per logarithmic frequency interval and normalized by the critical energy density) from our simulations expressed as  $h_0^2 \Omega_{\text{GW}}(f_{\text{phys}})$  for two families of models considered previously: one for the EW scale with  $k/H_\star = 600$  [49] and one for the QCD phase transition with  $k/H_\star = 6$  [64]. The former set of models is similar to simulations of Ref. [7], except that now we also consider models with stronger turbulent driving which is applied over one Hubble time along

<sup>2</sup> In the non-relativistic limit we obtain  $v_T = \sqrt{2\mathcal{E}_K/(\rho + P)}$  and  $v_A = B_{\text{eff}}/\sqrt{4\pi(\rho + P)} = \sqrt{2\mathcal{E}_M/(\rho + P)}$

with a period during which the forcing decreases linearly in time to zero, again over one Hubble time.

As already noted in previous studies [7, 8, 49], the GW energy spectrum from forced turbulence shows a rapidly declining inertial range for frequencies above the peak. This is because only the smallest wave numbers contribute significantly to the driving of GWs [49, 65]. The GW energy  $h_0^2 \Omega_{\text{GW}}(f_{\text{phys}})$  scales approximately quadratically with the ratio of magnetic energy to characteristic wave number  $k_0$  as  $(Q\mathcal{E}_M/k_0)^2$ , where  $Q$  is the GW efficiency (of order unity). For the QCD phase transition, the characteristic wave number is a hundred times smaller, so the GW energy is correspondingly larger.

Toward smaller frequencies, the spectra show a shallower fall-off, in some cases proportional to  $f_{\text{phys}}^{1.6}$ . This is steeper than what has been found in earlier simulations at lower magnetic energies, but shallower than what was generally expected based on analytical considerations. Physics beyond the SM often leads to parity symmetry breaking and correspondingly to polarized gravitational waves. In Figure 3 we show the polarization spectra,  $\mathcal{P}_{\text{GW}}(k) = \int 2 \text{Im} \tilde{h}_+ \tilde{h}_\times^* k^2 d\Omega_k / (\tilde{h}_+^2 + \tilde{h}_\times^2) k^2 d\Omega_k$ , for the same runs as in Figure 2; see also Eq. (B.17) in Ref. [66]. For the QCD phase transition with only a few bubbles per linear Hubble scale, the polarization spectra have an extended region with  $\mathcal{P}_{\text{GW}} \sim 1$ , while for

the electroweak phase transitions with tens of bubbles, the polarization spectra have non-trivial profiles with a narrower plateau.

In summary, BBN data do not limit the kinetic or magnetic energy density of the turbulence at the moment of its generation to be 10% of the radiation energy when the decay process is accounted for. Strong turbulence unavoidably results in a more powerful source for the GW signal with more optimistic prospects for GW detection.

**Data availability**—The source code used for the simulations of this study, the PENCIL CODE, is freely available from Refs. [54, 55]. The simulation setups and the corresponding data are freely available from Ref. [67].

**Acknowledgements**—Support through the Swedish Research Council, grant 2019-04234, and Shota Rustaveli NSF of Georgia (grant FR/18-1462) are gratefully acknowledged. Nordita is supported in part by Nordforsk. We acknowledge the allocation of computing resources provided by the Swedish National Infrastructure for Computing (SNIC) at the PDC Center for High Performance Computing Stockholm and the National Supercomputer Centre (NSC) at Linköping. J.S. acknowledges support from the Undergraduate Research Office in the form of a Summer Undergraduate Research Fellowship.

- 
- [1] C. Caprini and D. G. Figueroa, *Class. Quant. Grav.* **35**, 163001 (2018), arXiv:1801.04268.
  - [2] T. Kahniashvili, G. Gogoberidze, and B. Ratra, *Phys. Rev. Lett.* **95**, 151301 (2005), arXiv:astro-ph/0505628.
  - [3] S. Alexander, E. McDonough, and D. N. Spergel, *JCAP* **05**, 003 (2018), arXiv:1801.07255.
  - [4] S. Anand, J. R. Bhatt, and A. K. Pandey, *Eur. Phys. J. C* **79**, 119 (2019), arXiv:1801.00650.
  - [5] P. Niksa, M. Schlegeler, and G. Sigl, *Class. Quant. Grav.* **35**, 144001 (2018), arXiv:1803.02271.
  - [6] J. Ellis, M. Fairbairn, M. Lewicki, V. Vaskonen, and A. Wickens, *JCAP* **10**, 032 (2020), arXiv:2005.05278.
  - [7] T. Kahniashvili, A. Brandenburg, G. Gogoberidze, S. Mandal, and A. Roper Pol, *Phys. Rev. Res.* **3**, 013193 (2021), arXiv:2011.05556.
  - [8] A. Brandenburg, Y. He, T. Kahniashvili, M. Rheinhardt, and J. Schober, *Astrophys. J.* **911**, 110 (2021), arXiv:2101.08178.
  - [9] S. H.-S. Alexander, M. E. Peskin, and M. M. Sheikh-Jabbari, *Phys. Rev. Lett.* **96**, 081301 (2006), arXiv:hep-th/0403069.
  - [10] D. H. Lyth, C. Quimbay, and Y. Rodriguez, *JHEP* **03**, 016 (2005), arXiv:hep-th/0501153.
  - [11] A. Lue, L.-M. Wang, and M. Kamionkowski, *Phys. Rev. Lett.* **83**, 1506 (1999), arXiv:astro-ph/9812088.
  - [12] S. Alexander and N. Yunes, *Phys. Rept.* **480**, 1 (2009), arXiv:0907.2562.
  - [13] N. Bartolo, S. Matarrese, M. Peloso, and M. Shiraishi, *JCAP* **01**, 027 (2015), arXiv:1411.2521.
  - [14] P. Amaro-Seoane *et al.*, *Class. Quant. Grav.* **29**, 124016 (2012), arXiv:1202.0839.
  - [15] N. Seto and A. Taruya, *Phys. Rev. Lett.* **99**, 121101 (2007), arXiv:0707.0535.
  - [16] V. Domcke *et al.*, *JCAP* **05**, 028 (2020), arXiv:1910.08052.
  - [17] A. Roper Pol, S. Mandal, A. Brandenburg, and T. Kahniashvili, (2021), arXiv:2107.05356.
  - [18] M. Kusakabe, A. Kedia, G. J. Mathews, and N. Sasankan, *Phys. Rev. D* **104**, 123534 (2021).
  - [19] Y. Lu and M. Kusakabe, *Astrophys. J. Lett.* **926**, L4 (2022), arXiv:2201.13039.
  - [20] J. A. Frieman, E. W. Kolb, and M. S. Turner, *Phys. Rev. D* **41**, 3080 (1990).
  - [21] D. Grasso and H. R. Rubinstein, *Astropart. Phys.* **3**, 95 (1995), arXiv:astro-ph/9409010.
  - [22] G. M. Fuller and C. Y. Cardall, *Nucl. Phys. B Proc. Suppl.* **51**, 71 (1996), arXiv:astro-ph/9606025.
  - [23] K. Ichikawa and M. Kawasaki, *Phys. Rev. D* **69**, 123506 (2004), arXiv:hep-ph/0401231.
  - [24] V. Simha and G. Steigman, *JCAP* **06**, 016 (2008), arXiv:0803.3465.
  - [25] N. Sasankan, M. R. Gangopadhyay, G. J. Mathews, and M. Kusakabe, *Int. J. Mod. Phys. E* **26**, 1741007 (2017), arXiv:1706.03630.
  - [26] C. Keith, D. Hooper, N. Blinov, and S. D. McDermott, *Phys. Rev. D* **102**, 103512 (2020), arXiv:2006.03608.
  - [27] P. F. de Salas and S. Pastor, *JCAP* **07**, 051 (2016), arXiv:1606.06986.
  - [28] B. D. Fields, K. A. Olive, T.-H. Yeh, and C. Young, *Journal of Cosmology and Astroparticle Physics* **2020**, 010 (2020), arXiv:1912.01132.
  - [29] M. Benetti, L. L. Graef, and S. Vagnozzi, (2021),

- arXiv:2111.04758.
- [30] V. Simha and G. Steigman, *JCAP* **08**, 011 (2008), arXiv:0806.0179.
  - [31] A. Vilenkin, *Phys. Rev. D* **22**, 3080 (1980).
  - [32] Y. Luo, T. Kajino, M. Kusakabe, and G. J. Mathews, *Astrophys. J.* **872**, 172 (2019), arXiv:1810.08803.
  - [33] M. S. Turner and F. Wilczek, *Phys. Rev. Lett.* **65**, 3080 (1990).
  - [34] E. Witten, *Phys. Rev. D* **30**, 272 (1984).
  - [35] C. J. Hogan, *Mon. Not. Roy. Astron. Soc.* **218**, 629 (1986).
  - [36] M. Kamionkowski, A. Kosowsky, and M. S. Turner, *Phys. Rev. D* **49**, 2837 (1994), arXiv:astro-ph/9310044.
  - [37] A. Brandenburg, K. Enqvist, and P. Olesen, *Phys. Rev. D* **54**, 1291 (1996), arXiv:astro-ph/9602031.
  - [38] M. Christensson, M. Hindmarsh, and A. Brandenburg, *Phys. Rev. E* **64**, 056405 (2001), arXiv:astro-ph/0011321.
  - [39] T. Kahniashvili, A. Brandenburg, A. G. Tevzadze, and B. Ratra, *Phys. Rev. D* **81**, 123002 (2010), arXiv:1004.3084.
  - [40] A. Brandenburg *et al.*, *Phys. Rev. Fluids* **4**, 024608 (2019), arXiv:1710.01628.
  - [41] R. Durrer and A. Neronov, *Astron. Astrophys. Rev.* **21**, 62 (2013), arXiv:1303.7121.
  - [42] A. Kosowsky, A. Mack, and T. Kahniashvili, *Phys. Rev. D* **66**, 024030 (2002), arXiv:astro-ph/0111483.
  - [43] A. D. Dolgov, D. Grasso, and A. Nicolis, *Phys. Rev. D* **66**, 103505 (2002), arXiv:astro-ph/0206461.
  - [44] C. Caprini *et al.*, *JCAP* **03**, 024 (2020), arXiv:1910.13125.
  - [45] NANOGrav, Z. Arzoumanian *et al.*, *Astrophys. J. Lett.* **905**, L34 (2020), arXiv:2009.04496.
  - [46] J. Garcia-Bellido, H. Murayama, and G. White, (2021), arXiv:2104.04778.
  - [47] NANOGrav, Z. Arzoumanian *et al.*, (2021), arXiv:2104.13930.
  - [48] M. Ackermann *et al.*, *The Astrophysical Journal Supplement Series* **237**, 32 (2018).
  - [49] A. Roper Pol, S. Mandal, A. Brandenburg, T. Kahniashvili, and A. Kosowsky, *Phys. Rev. D* **102**, 083512 (2020), arXiv:1903.08585.
  - [50] A. Brandenburg *et al.*, *Phys. Rev. D* **96**, 123528 (2017), arXiv:1711.03804.
  - [51] See the supplemental material for the full set of equations and a summary of additional parameters of the simulations.
  - [52] T. Vachaspati, *Rept. Prog. Phys.* **84**, 074901 (2021), arXiv:2010.10525.
  - [53] J. Zrake and W. E. East, *Astrophys. J.* **817**, 89 (2016), arXiv:1509.00461.
  - [54] Pencil Code Collaboration *et al.*, *The Journal of Open Source Software* **6**, 2807 (2021).
  - [55] The pencil code. doi:10.5281/zenodo.2315093. <https://github.com/pencil-code>.
  - [56] T. Kahniashvili, L. Kisslinger, and T. Stevens, *Phys. Rev. D* **81**, 023004 (2010), arXiv:0905.0643.
  - [57] J. Ellis, M. Lewicki, and J. M. No, *JCAP* **04**, 003 (2019), arXiv:1809.08242.
  - [58] D. Bodeker, L. Fromme, S. J. Huber, and M. Seniuch, *JHEP* **02**, 026 (2005), arXiv:hep-ph/0412366.
  - [59] J. Choi and R. R. Volkas, *Phys. Lett. B* **317**, 385 (1993), arXiv:hep-ph/9308234.
  - [60] A. Nicolis, *Class. Quant. Grav.* **21**, L27 (2004), arXiv:gr-qc/0303084.
  - [61] M. Gedalin, *Phys. Rev. E* **47**, 4354 (1993).
  - [62] A. G. Riess *et al.*, *Astrophys. J.* **826**, 56 (2016), arXiv:1604.01424.
  - [63] Y. Nakai, M. Suzuki, F. Takahashi, and M. Yamada, *Phys. Lett. B* **816**, 136238 (2021), arXiv:2009.09754.
  - [64] A. Brandenburg, E. Clarke, Y. He, and T. Kahniashvili, *Phys. Rev. D* **104**, 043513 (2021), arXiv:2102.12428.
  - [65] A. Brandenburg *et al.*, *Class. Quant. Grav.* **38**, 145002 (2021), arXiv:2103.01140.
  - [66] A. Roper Pol, A. Brandenburg, T. Kahniashvili, A. Kosowsky, and S. Mandal, *Geophys. Astrophys. Fluid Dynamics* **114**, 130 (2020), arXiv:1807.05479.
  - [67] T. Kahniashvili, E. Clarke, J. Stepp, and A. Brandenburg, *Datasets for Big bang nucleosynthesis limits and relic gravitational waves detection prospects*, doi:10.5281/zenodo.5709176 (v2021.11.18); see also <http://www.nordita.org/~brandenb/projects/GWs-BBN/> for easier access .

# Supplementary Material to “Big Bang Nucleosynthesis Limits and Relic Gravitational Waves Detection Prospects”

## I. MAGNETIC FIELD BOUNDS

The bound on extra relativistic degrees of freedom at big bang nucleosynthesis (BBN) can be expressed as

$$\frac{\rho_B(T_{\text{BBN}})}{\rho_\gamma(T_{\text{BBN}})} = f, \quad (1)$$

where we have assumed that all the extra relativistic energy density is entirely due to the magnetic energy density  $\rho_B$ ,  $\rho_\gamma$  is the energy density in photons,  $T_{\text{BBN}}$  is the temperature of helium synthesis and  $f \equiv \frac{7}{8}(\frac{4}{11})^{4/3}\Delta N_{\text{eff}}$ .

The photon energy density as a function of temperature is  $\rho_\gamma = (\pi^2/15)T_\gamma^4$ . The magnetic energy density is related to the magnetic field strength  $B$  as  $\rho_B = B^2/8\pi$  (in Gaussian units). The magnetic field strength dilutes with the expansion of the universe as  $B \sim a^{-2}$  where  $a$  is the cosmological scale factor. The comoving magnetic field strength is given by  $B^{\text{co}} = (a/a_0)^2 B(a)$ , where  $a_0$  is the scale factor today. Substituting these values into the equation 1, the BBN limit on the field strength today is given by

$$B_*^{\text{co}} \leq \left(\frac{a_{\text{BBN}}}{a_0}\right)^2 \sqrt{8\pi f \rho_\gamma(T_{\text{BBN}})}. \quad (2)$$

Obtaining the ratio of the scale factors via entropy conservation, normalizing such that  $a_0 = 1$ , the bound is given by

$$\frac{B_*^{\text{co}}}{B_{\text{Gauss}}} \leq (8.06 \times 10^{-6}) f^{1/2} g_{\text{BBN}}^{-2/3} \quad (3)$$

where  $g_{\text{BBN}}$  is the relativistic degrees of freedom at  $T_{\text{BBN}}$ . There is no explicit dependence on temperature, however, the total number of relativistic degrees of freedom  $g_{\text{BBN}}$  does depend on the temperature. At  $T_{\text{BBN}} = 0.1$  MeV, the temperature at which deuterium synthesis starts, neutrinos have already decoupled, electrons and positrons have already become nonrelativistic, and  $g_{\text{BBN}}(T = 0.1\text{MeV}) \simeq 3.4$ . For  $\Delta N_{\text{eff}} = 0.122$ , we find  $f = 0.028$  and the maximum comoving field strength at BBN is  $B_{\text{BBN}}^{\text{max}} = 6.2 \times 10^{-7}$  G.

## II. NUMERICAL SET-UP/GRAVITATIONAL WAVES

We consider the radiation-dominated epoch at electroweak (EW) and quantum chromodynamic (QCD) energy scales and compute the strains  $h_+$  and  $h_\times$  for the two linear polarization modes by solving the linearized equation for gravitational waves (GWs),

$$\frac{\partial^2}{\partial t^2} \tilde{h}_{+/\times} + \mathbf{k}^2 \tilde{h}_{+/\times} = \frac{6}{a} \tilde{T}_{+/\times}, \quad (4)$$

where  $\tilde{T}_{+/\times}$  are the  $+$  and  $\times$  polarizations of the Fourier transform of the total stress  $\mathbf{T}_{ij} = u_i u_j - B_i B_j$ , normalized by the radiation energy density, with  $t$  and  $\mathbf{k}$  the time and wave vector normalized by the Hubble parameter at the time of generation, and  $\mathbf{B} = \nabla \times \mathbf{A}$  and  $\mathbf{u}$  are obtained by solving the equation for the magnetic vector potential

$$\frac{\partial \mathbf{A}}{\partial t} = \mathbf{u} \times \mathbf{B} + \eta \nabla^2 \mathbf{A}, \quad (5)$$

together with [37]

$$\frac{\partial \mathbf{u}}{\partial t} = -\mathbf{u} \cdot \nabla \mathbf{u} - \frac{1}{4} \nabla \ln \rho + \frac{3}{4\rho} \mathbf{J} \times \mathbf{B} + \mathcal{F}_\nu + \mathcal{F}, \quad (6)$$

$$\frac{\partial \ln \rho}{\partial t} = -\frac{4}{3} (\nabla \cdot \mathbf{u} + \mathbf{u} \cdot \nabla \ln \rho) + \mathcal{H}, \quad (7)$$

where  $\mathcal{F} = (\nabla \cdot \mathbf{u} + \mathbf{u} \cdot \nabla \ln \rho) \mathbf{u} / 3 - [\mathbf{u} \cdot (\mathbf{J} \times \mathbf{B}) + \mathbf{J}^2 / \sigma] \mathbf{u} / \rho$ , and  $\mathcal{H} = [\mathbf{u} \cdot (\mathbf{J} \times \mathbf{B}) + \mathbf{J}^2 / \sigma] \rho$  are higher order terms in the Lorentz factor that are retained in the calculation, and  $\mathcal{F}_\nu = 2\nabla \cdot (\rho \nu \mathbf{S}) / \rho$  is the viscous force, where  $\mathbf{S}_{ij} = \frac{1}{2}(u_{i,j} + u_{j,i}) - \frac{1}{3}\delta_{ij} \nabla \cdot \mathbf{u}$  are the components of the rate-of-strain tensor with commas denoting partial derivatives, and  $\nu$  is the kinematic viscosity. In all cases considered below, we assume a magnetic Prandtl number of unity, i.e.,  $\nu/\eta = 1$ . In Table I, we summarize the parameters for runs a-d and A-D for the QCD and EW energy scales, respectively. Here,  $h_{\text{rms}}^{\text{sat}}$  refers to the value of  $\langle h_+^2 + h_\times^2 \rangle^{1/2}$  evaluated during the final stationary regime.

As in Ref. [7], hereafter K+21, we compute GW generation from magnetically driven turbulence. The driving is applied during the time interval  $1 \leq t \leq 2$ , where  $t$  is the conformal time. As in K+21, we then decrease the driving linearly in time until  $t = 3$ , when the driving is turned off completely. We perform series of runs where we vary the strength of the forcing  $f_0$  and keep the viscosity  $\nu$  unchanged. However, it is not possible to explore the regime of strong magnetic energy at the same small values of  $\nu$  that we were able to use for smaller magnetic energies. This is because for strong magnetic fields, the turbulence becomes more intense and more viscosity is needed to dissipate all this energy at the finite numerical resolution available.

In Fig. 4, we show the resulting dependence of the GW energy  $\mathcal{E}_{\text{GW}}$  on the magnetic energy  $\mathcal{E}_{\text{M}}$  for six sets of runs with fixed viscosity, different forcing strengths, and different forcing wavenumbers, corresponding to the runs denoted with labels a-d, A-D, and O. In all cases, we take the magnetic Prandtl number to be unity, i.e., the magnetic diffusivity is set equal to the value of  $\nu$ . We also compare with several other sets of runs where we change the forcing.

In Table I, we summarize the parameters for four runs (A-D), which correspond to the less viscous ones for each of the four pairs shown in Fig. 4. One exception is Run D, which has the same viscosity as Run C and is denoted in

TABLE I: Summary of the runs.

Run	$f_0$	$\nu$	$\mathcal{E}_M^{\max}$	$\mathcal{E}_{\text{GW}}^{\text{sat}}$	$h_{\text{rms}}^{\text{sat}}$	$B_{\text{rms}} [\mu\text{G}]$	$h_0^2 \Omega_{\text{GW}}$	$h_c$
Fa	$5 \times 10^{-1}$	$2 \times 10^{-2}$	$1.40 \times 10^{-0}$	$2.6 \times 10^{-1}$	$2.7 \times 10^{-1}$	4.7	$8.04 \times 10^{-6}$	$2.69 \times 10^{-13}$
a2	$3 \times 10^{-1}$	$2 \times 10^{-2}$	$5.08 \times 10^{-1}$	$3.0 \times 10^{-2}$	$9.2 \times 10^{-2}$	2.9	$9.19 \times 10^{-7}$	$9.19 \times 10^{-14}$
b	$3 \times 10^{-1}$	$5 \times 10^{-3}$	$9.40 \times 10^{-1}$	$5.4 \times 10^{-2}$	$1.4 \times 10^{-1}$	3.9	$1.66 \times 10^{-6}$	$1.36 \times 10^{-13}$
c	$2 \times 10^{-1}$	$5 \times 10^{-3}$	$4.26 \times 10^{-1}$	$9.4 \times 10^{-3}$	$5.7 \times 10^{-2}$	2.6	$2.90 \times 10^{-7}$	$5.73 \times 10^{-14}$
d	$1 \times 10^{-1}$	$5 \times 10^{-3}$	$1.09 \times 10^{-1}$	$5.5 \times 10^{-4}$	$1.4 \times 10^{-2}$	1.3	$1.71 \times 10^{-8}$	$1.38 \times 10^{-14}$
A	$7 \times 10^{-3}$	$5 \times 10^{-5}$	$4.05 \times 10^{-1}$	$3.0 \times 10^{-5}$	$3.1 \times 10^{-5}$	2.5	$4.93 \times 10^{-10}$	$2.46 \times 10^{-20}$
A'	$7 \times 10^{-3}$	$5 \times 10^{-5}$	$3.94 \times 10^{-1}$	$2.4 \times 10^{-5}$	$2.7 \times 10^{-5}$	2.5	$3.91 \times 10^{-10}$	$2.19 \times 10^{-20}$
A2	$7 \times 10^{-3}$	$1 \times 10^{-4}$	$1.91 \times 10^{-1}$	$9.5 \times 10^{-6}$	$2.0 \times 10^{-5}$	1.8	$1.56 \times 10^{-10}$	$1.61 \times 10^{-20}$
O1	$5 \times 10^{-3}$	$5 \times 10^{-5}$	$1.82 \times 10^{-1}$	$5.4 \times 10^{-6}$	$1.4 \times 10^{-5}$	1.7	$8.86 \times 10^{-11}$	$1.12 \times 10^{-20}$
O1'	$5 \times 10^{-3}$	$5 \times 10^{-5}$	$1.74 \times 10^{-1}$	$4.3 \times 10^{-6}$	$1.2 \times 10^{-5}$	1.7	$7.07 \times 10^{-11}$	$9.65 \times 10^{-21}$
O2	$5 \times 10^{-3}$	$1 \times 10^{-4}$	$7.50 \times 10^{-2}$	$1.7 \times 10^{-6}$	$8.4 \times 10^{-6}$	1.1	$2.84 \times 10^{-11}$	$6.67 \times 10^{-21}$
B	$2 \times 10^{-3}$	$2 \times 10^{-6}$	$9.67 \times 10^{-2}$	$5.6 \times 10^{-7}$	$5.2 \times 10^{-6}$	1.2	$9.24 \times 10^{-12}$	$4.17 \times 10^{-21}$
C2	$1 \times 10^{-3}$	$2 \times 10^{-6}$	$2.74 \times 10^{-2}$	$3.1 \times 10^{-8}$	$1.3 \times 10^{-6}$	0.66	$5.03 \times 10^{-13}$	$1.03 \times 10^{-21}$
C	$1 \times 10^{-3}$	$2 \times 10^{-7}$	$3.35 \times 10^{-2}$	$3.5 \times 10^{-8}$	$1.3 \times 10^{-6}$	0.73	$5.80 \times 10^{-13}$	$1.07 \times 10^{-21}$
D	$6 \times 10^{-4}$	$2 \times 10^{-7}$	$1.68 \times 10^{-2}$	$5.3 \times 10^{-9}$	$7.1 \times 10^{-7}$	0.52	$8.73 \times 10^{-14}$	$5.64 \times 10^{-22}$

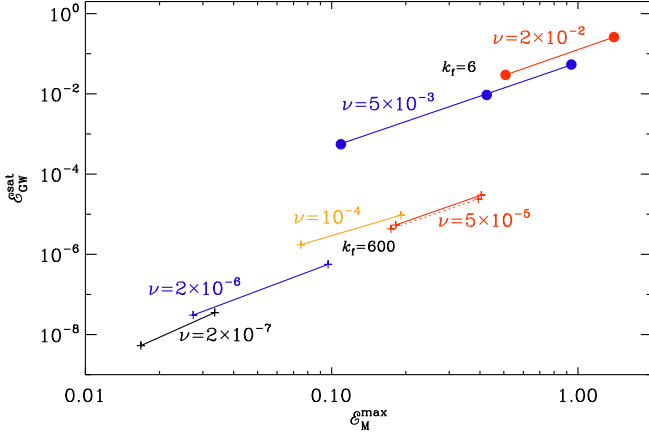


FIG. 4: Dependence of  $\mathcal{E}_{\text{GW}}^{\text{sat}}$  on  $\mathcal{E}_M^{\text{max}}$  for magnetically driven turbulence at different forcing strengths and viscosities for  $k_f = 6$  (upper red and blue lines) and  $k_f = 600$  (lower red, orange, blue, and black lines). The red dashed line for  $k_f = 600$  denotes runs where the driving is turned off abruptly at  $t = 2$ .

Fig. 4 by a red line. Run D is the same one as Run M1 of K+21. The values of  $\mathcal{E}_M$  and  $\mathcal{E}_{\text{GW}}$  agree with those of K+21 for this run, but those of  $h_{\text{rms}}$  are here a bit smaller. In fact, a closer inspection of the time series of  $h_{\text{rms}}(t)$  revealed that it reaches a steady state much later than  $\mathcal{E}_{\text{GW}}(t)$ . Therefore, averaging can begin only later than for  $\mathcal{E}_{\text{GW}}$ . Since  $h_{\text{rms}}$  is found to decrease somewhat after having reached a maximum, the new value in Table I is now about 20% smaller than that given in K+21.

The data for  $\mathcal{E}_{\text{GW}}$  follow a power law scaling,  $\propto \mathcal{E}_M^n$ , where  $n = 2.7$  for the points with the smallest viscosity.

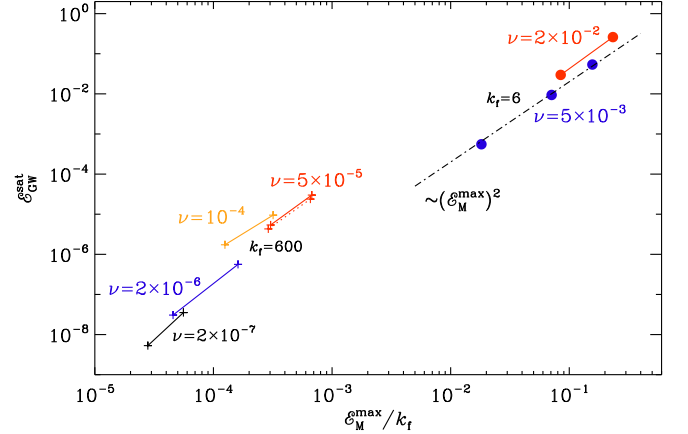


FIG. 5: Dependence of  $\mathcal{E}_{\text{GW}}^{\text{sat}}$  on  $\mathcal{E}_M^{\text{max}}/k_f$  for the same runs as in Fig. 4.

This is steeper than the quadratic scaling found in the work of [49], where the driving was applied for a much shorter time interval,  $1 \leq t \leq 1.1$ . Furthermore, for fixed values of  $\nu$ , we find smaller local values of  $n$ , at least for the larger magnetic energies shown in Fig. 4. We also checked that these scalings are not significantly affected if the driving was turned off abruptly after  $t = 2$ . This is shown as the dotted line in Fig. 4 for  $\nu = 5 \times 10^{-5}$ .

Comparing the lines for  $\nu = 5 \times 10^{-5}$  and  $\nu = 10^{-4}$  in Figs. 4 and 5, we see that the decline of  $\mathcal{E}_M$  is stronger than that of  $\mathcal{E}_{\text{GW}}$ . This suggests that  $\mathcal{E}_M$  suffers more strongly from the increase of viscosity and magnetic diffusivity, and that  $\mathcal{E}_{\text{GW}}$  is less sensitive to the change of  $\nu$ . However, one has to remember that GWs are solely the result of the magnetic and hydrodynamic stresses. One

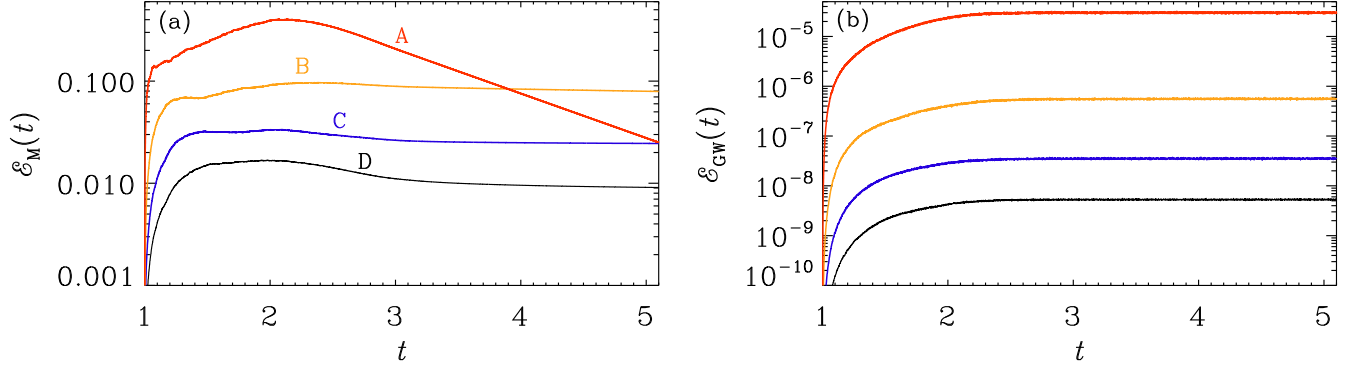


FIG. 6: Evolution of (a)  $\mathcal{E}_M(t)$  and (b)  $\mathcal{E}_{GW}(t)$  for Runs A–D of Table I. Note the rapid decay for Run A with the largest viscosity.

sees that the runs with smaller values of  $\nu$  all have a faster rise of  $\mathcal{E}_M(t)$  early on, which also translates into a rapid increase of  $\mathcal{E}_{GW}(t)$ . It is unclear, however, whether this aspect of the model with applied magnetic driving is realistic and whether this would also be borne out by a more physical implementation of a magnetogenesis model.

Next, we show in Fig. 6 the evolution of  $\mathcal{E}_M(t)$  and  $\mathcal{E}_{GW}(t)$  with time. We see that for Runs C and D,  $\mathcal{E}_M$

has reached a plateau well before  $t = 2$ , while for Run A, a maximum is reached only at  $t = 2$ , i.e., the time when the driving is decreased. Moreover, for Run A, there is a strong temporal decline of magnetic energy due to strong viscous damping. Nevertheless, similar GW energies are obtained in this case. The value of  $\mathcal{E}_{GW} = 3 \times 10^{-5}$  given in Table I corresponds to  $h_0^2 \Omega_{GW} = 4.93 \times 10^{-10}$ , which is four orders of magnitude larger than for Run D.